(Received 10 June 2025, Accepted 10 July 2025, Scheduled 26 July 2025)

Permanent Magnet Assisted Switched Reluctance Motor DITC Control Based on Current-Torque Synergy

Junjie Zhang, Junxin Xu*, Chaozhi Huang, Ziyang Liu, Yiqiang Yu, and Pengpeng Wei

School of Electrical Engineering and Automation, Jiangxi University of Science and Technology, Ganzhou 341000, Jiangxi, China

ABSTRACT: Permanent magnet-assisted reluctance motors are characterized by high energy efficiency, high power density, and high speed-regulation range, but the high peak excitation current and large torque ripple of their traditional direct instantaneous torque control (DITC) strategy limit the development and application of the motors. Therefore, this paper proposes a new DITC strategy based on Current-Torque Synergy, which firstly divides the intervals according to the characteristics of the inductance curve, and different intervals are used with a compatible hysteresis loop method. Then for the problem of high peak excitation current, introduce current chopper control and design the reference current value adaptive adjustment algorithm, realize the control of the excitation phase current according to the motor speed and load size at the beginning of the phase change, and suppress the current peak during the phase change. Finally, a three-phase 6/20 permanent magnet-assisted switched reluctance motor is taken as the research object for simulation analysis and prototype experiment. The results show that the proposed control strategy can effectively reduce the current peak and improve the torque output capability and dynamic response capability during phase change.

1. INTRODUCTION

Permanent magnet-assisted switched reluctance motors (PMa-SRMs) have attracted extensive attention from many scholars due to their advantages such as simple structure, high reliability, low cost, and strong fault-tolerant capability [1–3]. However, the highly nonlinear magnetic circuit characteristics caused by this special doubly salient pole structure [4, 5] lead to significant torque ripple during motor operation, limiting its popularization and application in industry.

At present, methods for suppressing torque ripple in reluctance motors mainly focus on two aspects: structure and control. From the structure, [6–8] aim to suppress torque ripple by modifying the motor's inherent structure, such as adding grooves or optimizing the stator-rotor structure, but increased the structural complexity as well as manufacturing cost, while making the motor reliability reduced. Ref. [9] reduces torque ripple by using a triangular lamination of rotor silicon steel with axial middle skewed slots and reverse skewed slots, and Ref. [10] uniformly adds eight spring supports between the motor casing and stator yoke to buffer the impact of the stator core on the casing transmitted by stator teeth and reduce torque ripple. From the control, Ref. [11] proposes a current chopping control method with reference current compensation to enhance torque output capability and dynamic response during commutation, though its compensation effect is limited, and implementation is difficult. Ref. [12] borrows the dq-axis control concept from synchronous motors to non-negatively process and correct reference currents based on current and inductance characteristics, ensuring smooth torque output. Ref. [13] introduces current feedback into traditional direct instantaneous torque control (DITC) to suppress current pulses while controlling torque, achieving stable torque output, but requiring higher computational effort. Refs. [14–16] divide the two-phase commutation region into four intervals, propose hysteresis control strategies adapted to interval inductance, and combine turn-on or turn-off angle optimization algorithms to effectively reduce torque ripple across a wide speed range. Ref. [17] presents a current prediction method based on torque distribution functions to improve position and current tracking accuracy, addressing large torque ripple caused by weak current tracking capability at high speeds.

The traditional DITC is prone to generating current pulses at the initial stage of commutation, leading to excessive output torque ripple. To address this issue, this paper proposes a current-torque synergy DITC strategy. First, the rotor position is divided into intervals based on the inductance characteristics of the PMa-SRM, with different control methods applied in each interval. Meanwhile, current feedback is introduced as one of the criteria for switch conduction to control the exciting phase current according to the motor speed and load. By controlling the exciting current, torque ripple is reduced, thereby improving the system's operational efficiency. Finally, simulations and prototype experiments are conducted to validate the proposed control method.

2. TRADITIONAL DITC STRATEGY

Traditional DITC achieves effective torque regulation solely based on instantaneous torque parameters, featuring a simple and flexible control scheme with excellent dynamic and static characteristics. The system block diagram of the traditional DITC is shown in Fig. 1. The speed error between the refer-

* Corresponding author: Junxin Xu (xujx9997@163.com).

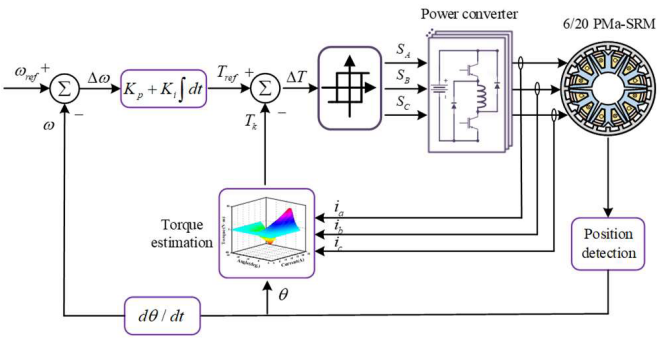

FIGURE 1. The system block diagram of the traditional DITC.

ence rotational speed ω_{ref} and the measured actual speed ω is processed by a proportional-integral (PI) controller to generate the desired torque T_{ref}. Concurrently, the current signal i and rotor position signal θ, acquired through the sensing module, are fed into the torque estimation module. The system then calculates the torque deviation ΔT ($\Delta T = T_{ref} - T_k$), where T_k denotes the estimated actual torque from the torque estimation module. Finally, based on the torque deviation ΔT, the torque hysteresis controller is controlled to output switching signals to drive the power converter, thereby achieving stable operation of the motor.

2.1. Principle of Instantaneous Torque Modulation

As shown in Fig. 2, the operation of the PMa-SRM follows the minimum reluctance principle, where each phase winding is sequentially energized, The phase commutation is achieved by controlling the power converter in the drive circuit. Based on the virtual work principle, the electromagnetic torque in the k-th phase winding can be approximated as:

$$T_k(i_k, \theta) = \frac{1}{2} i_k^2 \times \frac{dL_k(i_k, \theta)}{d\theta} \tag{1}$$

The inductance L_k (i_k, θ) is a function of the phase current i and rotor position angle θ. During motor operation, the rotor position angle θ cannot be actively regulated. Therefore, the phase torque is primarily controlled by adjusting the phase current i_k.

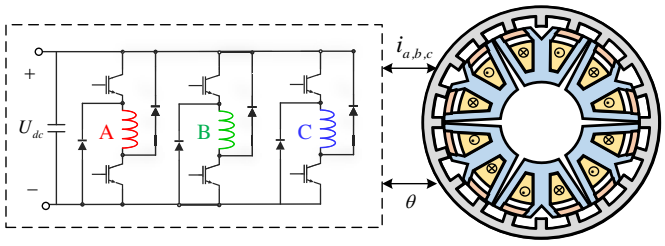

FIGURE 2. Planar structure and drive circuit of 6/20 pole motor.

The drive circuit typically employs a three-phase asymmetric half-bridge power converter, and the voltage balance equation between phase windings is expressed as:

$$U_k = R_k i_k + L_k \frac{di_k}{dt} + i_k \omega_r \frac{dL_k}{d\theta} \tag{2}$$

where U_k is the applied voltage, R_i the winding resistance, and ω_r the motor speed. Neglecting the voltage drop across the winding resistance, the rate of change of the phase current can be derived from Equation (2) as:

$$\frac{di_k}{dt} = \frac{U_k - i_k \omega_r \frac{dL_k}{d\theta}}{L_k} \tag{3}$$

As shown in Equation (3), adjusting the winding voltage alters the rate of change of the phase current, thereby modifying the current magnitude at the next time step to achieve torque control. Illustrated in Fig. 3, the power converter operates in three distinct states: magnetization, current continuation, and demagnetization, corresponding to terminal voltages of $+U_{dc}$, 0, and $-U_{dc}$ across the winding. By switching among these three operating states, the phase current is regulated, thereby enabling precise control of the motor's output torque.

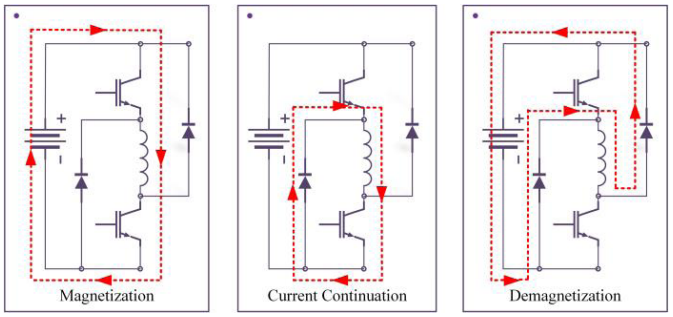

FIGURE 3. Three operating states of asymmetric half-bridge power converter.

In traditional DITC, the electrical cycle is partitioned into a Two-Phase Exchange (TpE) region and a Single-Phase Conduction (SpC) region based on rotor position. Distinct hysteresis strategies are employed in different inductance regions, as illustrated in Fig. 4. The switching states "1, 0, −1" represent the three operating modes of the power converter: excitation, freewheeling, and demagnetization. Here, T_L denotes the inner hysteresis threshold and T_H the outer hysteresis threshold. The torque error ΔT governs the switching logic of the power converter, expressed as:

$$\Delta T = T_{ref} - T_k \tag{4}$$

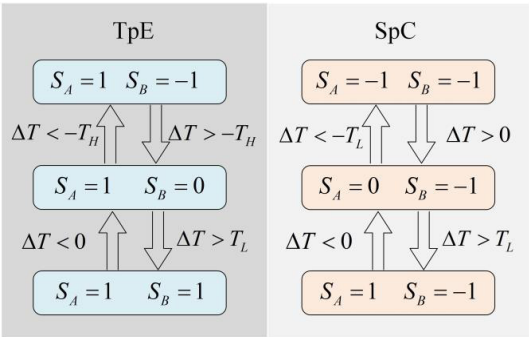

FIGURE 4. Traditional DITC two-phase exchange zone hysteresis loop rule.

Here, T_{ref} and T_k represent the reference torque and actual output torque, respectively.

In the TpE, the excitation phase remains continuously energized, while the demagnetization phase is governed by dual-loop alternating control. When the torque error ΔT exceeds the inner-loop threshold T_L, the demagnetization phase enters the excitation state. Conversely, when ΔT falls below the outer-loop threshold T_H, it switches to the demagnetization state. In the SpC, the excitation phase is primarily regulated by the inner-loop control. The phase transitions to the demagnetization state only when ΔT drops below the inner-loop threshold $-T_L$, enabling rapid torque reduction. Through this switching logic, the torque error is confined within a defined range, thereby effectively suppressing motor torque ripple.

2.2. Challenges in Traditional DITC

As shown in Fig. 5, during the first half of the TpE region, both the current and the rate of inductance change $dL/d\theta$ in the excitation phase are relatively small. Consequently, the electromagnetic torque generated during this interval is negligible. To rapidly build up the phase current, the excitation phase is primarily maintained in the energized state. However, conventional DITC relies solely on the torque error ΔT as the switching criterion, which frequently leads to current overshoot. Simultaneously, the rate of inductance change in the demagnetization phase gradually decreases, resulting in a weakened torque output capability. This asymmetric evolution of interphase torque characteristics causes the torque contribution from the excitation phase to be insufficient to compensate for the diminishing torque from the demagnetization phase. Ultimately, this imbalance induces a torque trough in the total synthesized torque. In the latter half of the TpE region, after reaching the inductance boundary point, the rate of inductance change $dL/d\theta$ in the excitation phase increases abruptly. The excessive current accumulated in the first half triggers a rapid surge in electromagnetic torque, leading to significant fluctuations in the three-phase synthesized torque.

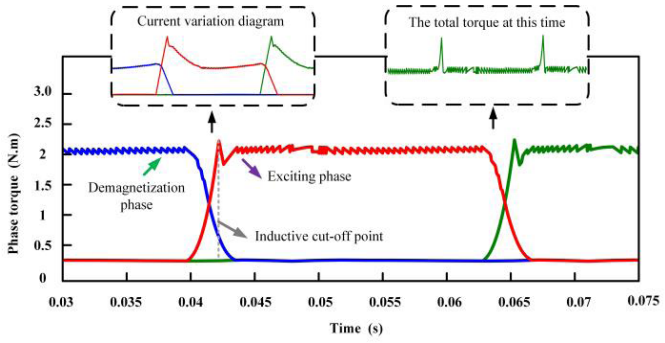

FIGURE 5. Phase torque and current waveforms during commutation in traditional DITC.

Traditional DITC employs distinct hysteresis strategies in different operational regions, demonstrating favorable control characteristics for torque ripple suppression. However, these hysteresis strategies solely utilize the torque error ΔT as the triggering criterion for power switching devices, rendering them ineffective in mitigating pulse current transients during dynamic motor operations. This limitation leads to spike distortion in phase current waveforms, which not only risks damaging switching devices but also degrades system efficiency. Furthermore, under certain conditions, it exacerbates the challenges of torque ripple suppression.

3. CURRENT-TORQUE SYNERGY DITC STRATEGY

To address the insufficient torque ripple suppression performance of traditional DITC strategies, this paper proposes a Current-Torque Synergy DITC strategy. The proposed control strategy first repartitions the operational regions based on the motor's inductance profile $L(\theta, i)$. New hysteresis strategies are designed for the demagnetization and excitation phases within different regions. To suppress spike distortion in phase current waveforms, the updated regional hysteresis strategy incorporates current error as an additional criterion for determining the switching states of power devices. Furthermore, to adapt to varying operating conditions, a Genetic Algorithm-Backpropagation (GA-BP) neural network-based adaptive controller dynamically adjusts the reference peak current i_{ref} for the next excitation phase. This approach simultaneously suppresses torque ripple and reduces current peaks, thereby enhancing system reliability and improving operational efficiency. The overall control architecture is illustrated in Fig. 6.

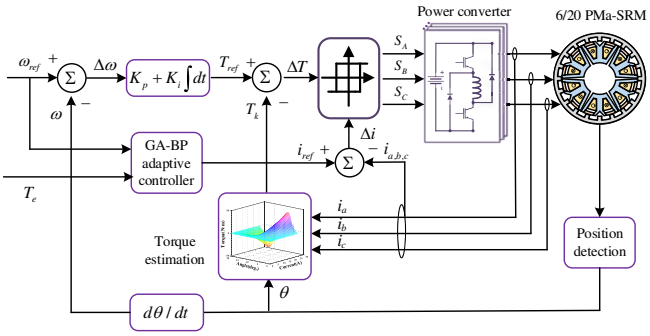

FIGURE 6. The system block diagram of the current-torque synergy DITC.

3.1. Current-Torque Synergy Regional Hysteresis Control

According to Equation (1), the instantaneous output torque of an SRM is related to its current magnitude and the rate of inductance variation. Therefore, to improve the torque ripple suppression performance of the control strategy, the original two-phase commutation region is further subdivided into Commutation Zone I and Commutation Zone II [18] based on the inductance characteristic curve. A corresponding hysteresis control method is then designed for the excitation phase and demagnetization phase in each zone, as illustrated in Fig. 7.

Taking the commutation process of phases A and B as an example, the single-phase conduction region is the area between the aligned position of phase A (θ_e^A) and the turn-on angle of phase B (θ_{on}^B). At this time, the inductance change rate of phase C is negative, and it should be maintained in the "-1" state to prevent the generation of negative torque. The inductance

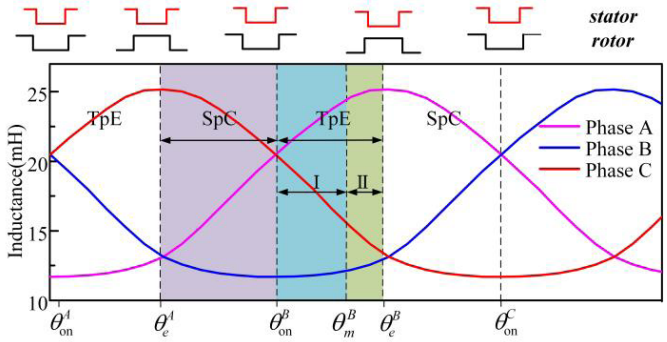

FIGURE 7. Schematic diagram of inductance characteristics and interval division.

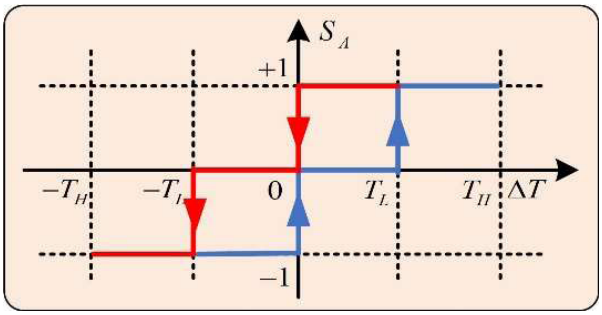

FIGURE 8. Hysteresis control method for phase a in single-phase conduction region.

change rate of phase A has reached its maximum value, and the output torque is provided by the conduction of phase A. The hysteresis strategy for phase A is shown in Fig. 8.

Commutation Zone I spans from the turn-on angle of phase B (θ_{on}^{B}) to the inductance boundary point (θ_{m}^{B}). In this zone, phase A exhibits a high inductance change rate and has established a sufficiently large current, while phase B has an almost zero inductance change rate and a small current amplitude. According to the torque output characteristics, phase A provides the main output torque at this time. Meanwhile, phase B has weak torque output capability in this zone and should be maintained in the "1" state as much as possible to quickly build up current. However, phase B has a small inductance and a fast current rise rate, which tends to generate current pulses. Therefore, based on the different inductance characteristics of the two phases, current chopping control is applied to phase B, and torque hysteresis control is applied to phase A in this zone.

Current chopping control restricts the phase current to fluctuate within a certain range through the given current upper limit value i_H and lower limit value i_h. The analytical expressions for the current upper limit value i_H and lower limit value i_h are:

$$\begin{cases} i_H = i_{ref} + 0.5h \\ i_L = i_{ref} - 0.5h \end{cases} \tag{5}$$

In the formula: i_{ref} is the reference current value, which is related to the rotational speed and load during operation. The schematic diagram of the current chopping control process is shown in Fig. 9. When phase B is turned on, G_1 and G_2 are

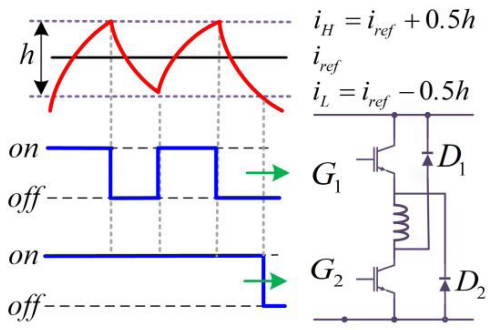

FIGURE 9. Schematic diagram of current chopping control process.

closed, and the current rises rapidly. When the current of phase B reaches the upper limit value i_H, G_2 is turned off; the winding is in a zero-voltage freewheeling state; and the current decreases slowly. When the current of phase B drops to the lower limit value i_h, G_2 is closed again, and the current rises. The hysteresis rule for phase B in this zone is shown in Fig. 10. By adjusting the switching states of power devices, the current is kept fluctuating around the reference current value, overcoming the problem of excessively large peak current in traditional DITC.

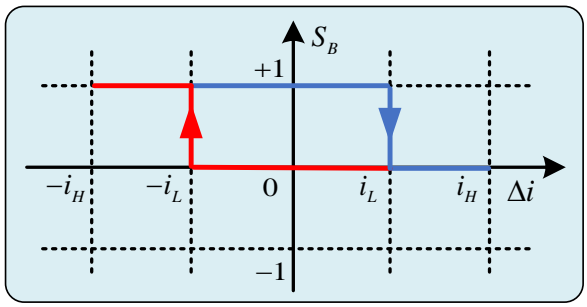

FIGURE 10. Hysteresis current control method for phase B in commutation zone I.

In the entire Commutation Zone I, phase A serves as the main torque output phase. At this time, the torque hysteresis control strategy shown in Fig. 8 is adopted. By changing the operating states of power devices, the torque deviation is constrained within the range of $-\Delta T$ to ΔT. During the entire control process, when the current control of phase B causes torque fluctuations, phase A with stronger torque regulation capability can correspondingly adjust its own torque output for compensation, thereby achieving smooth control of the total torque.

Commutation Zone II is the region from the inductance boundary point of phase B (θ_{m}^{B}) to the maximum inductance point of phase B (θ_{e}^{B}). At this stage, the inductance change rate of phase B increases and gradually exceeds that of phase A, enhancing its torque output capability while building up a sufficiently large current to meet the actual torque demand independently. Conversely, the inductance change rate of phase A continues to decrease, weakening its torque output capability. In this zone, phase B serves as the main torque output phase and adopts the same hysteresis strategy as phase A in Commutation Zone I. As the inductance of phase A approaches its maximum

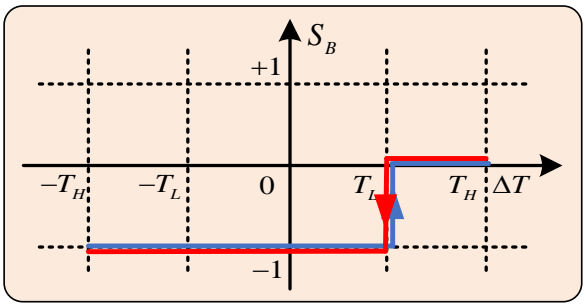

FIGURE 11. Hysteresis control method for phase A in commutation zone II.

value, it should preferably remain in the "−1" state and only switch to state "0" when the torque deviation exceeds ΔT to compensate for insufficient total torque output. The hysteresis strategy is shown in Fig. 11. Compared with traditional DITC, the strategy proposed in this paper allows phase A to retain certain torque regulation capability, enabling it to respond to external disturbances and improve the stability of motor operation.

3.2. Acquisition of Reference Current Value Parameters

As the core of current chopping control, the setting of the reference current value is crucial for system performance. Fig. 12 shows the torque ripple caused by different reference currents at the inductance boundary point. As known from equation (1), the magnitude of torque is the result of the interaction between the square of the current and the inductance change rate. Since the inductance boundary point is located where the inductance change rate increases sharply, excessively large exciting current here will cause an instantaneous surge in torque, forming sharp torque pulses. Conversely, too small an exciting current will limit the current square term, making it difficult to fully amplify the mutation effect of the inductance change rate, leading to insufficient torque output. Therefore, for different speeds and loads, selecting an appropriate reference current is crucial to reducing motor torque ripple and improving motor efficiency.

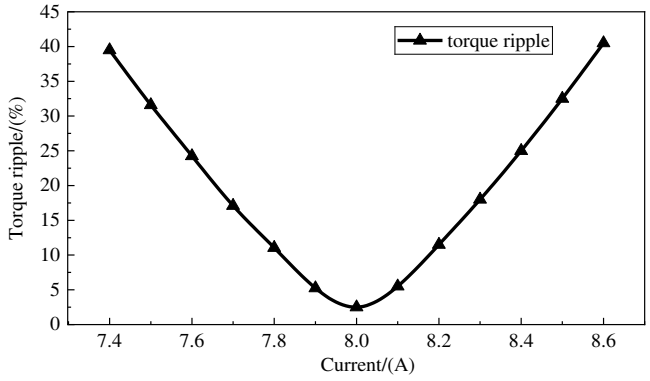

FIGURE 12. Relationship between different reference currents at inductance boundary point and torque ripple.

To this end, this paper employs a current parameter optimization algorithm based on GA-BP (Genetic Algorithm-Backpropagation Algorithm), which is an optimization algorithm combining genetic algorithms and backpropagation neural networks. Commonly used in data fitting, it can quickly obtain output values closest to the actual ones through training when input values are known, making it suitable for systems with complex internal mechanisms. The structure of the three-layer BP neural network is shown in Fig. 13.

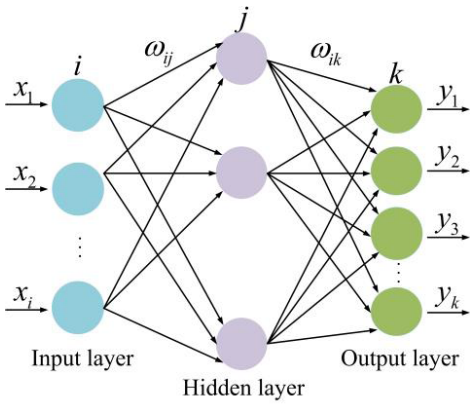

FIGURE 13. Schematic diagram of BP neural network structure.

The output analytical expressions of each layer are:

$$\begin{cases} u_i = x_i & \text{Input layer} \\ \mathbf{u}_j = \mathrm{f}\left(\sum_{i=1}^{m} \omega_{ij} x_i + \theta_j\right) & \text{Hidden layer} \\ \mathbf{u}_k = \mathrm{f}\left(\sum_{j=1}^{p} \omega_{jk} x_j \cdot f\left(\sum_{i=1}^{m} \omega_{ij} x_i + \theta_j\right) + \theta_k\right) & \text{Output layer} \end{cases} \tag{6}$$

Among them, the number of neurons in the input layer, hidden layer, and output layer are denoted as i, j, and k, respectively. The connection weight matrix between the input layer and hidden layer is denoted as w_{ij}, while the connection weight matrix between the hidden layer and output layer is denoted as w_{jk}.

Build the structural model of $i_{ref}(T, w)$ according to this algorithm. In this structure, the rotational speed and load torque are taken as the inputs of the input layer, and i_{ref} is the output of the output layer. The sampling range of the rotational speed is 200∼1000 r/min with a step size of 100 r/min, and the value range of the load torque is 2∼10 N·m with a step size of 1 N·m. Aiming at minimizing the torque ripple, the optimal i_{ref} of the motor under different working conditions is obtained through simulation experiments, and finally 81 sets of data are obtained. The distribution of the data is shown in Fig. 14.

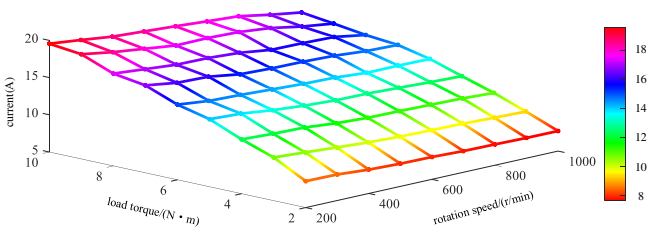

FIGURE 14. Data sample distribution diagram.

Divide the data into 64 sets of training data and 18 sets of test data. The GA-BP (Genetic Algorithm — Backpropagation) is used to predict parameters of the control strategy. The

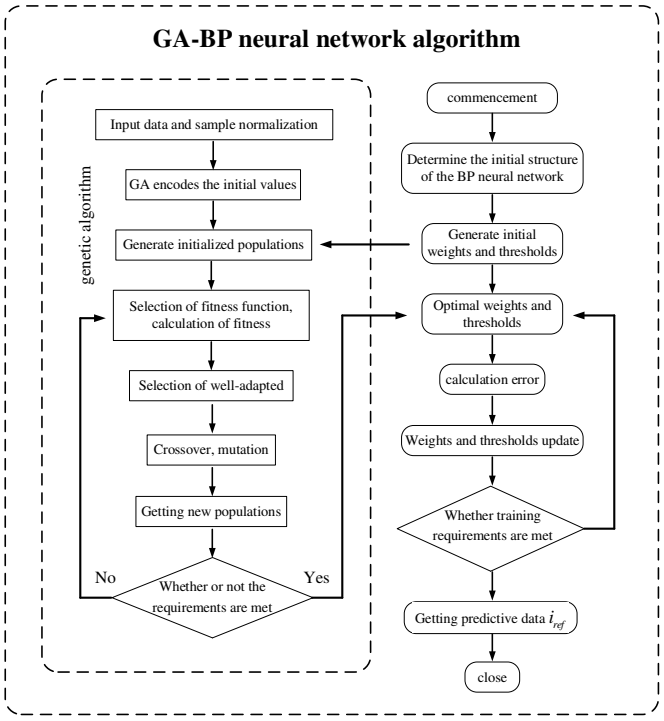

FIGURE 15. Flowchart of the whole process of GA-BP training.

flowchart is shown in Fig. 15. First, the input data are normalized, and the initial structure of the BP network is determined. The initial weights and thresholds are generated, then the initial values are encoded. The population is generated, and the fitness function is calculated and selected. Then the new population is obtained through crossover and mutation, and the cycle is repeated until it meets the requirements. The optimal weights and thresholds are output, and finally, the optimized parameters are used to calculate the error, update the weight thresholds, and determine whether the training requirements are met. If they meet the standards, then output the predicted data, and the process end.

The prediction accuracy of the model can be evaluated using the Root Mean Square Error (RMSE) index, where a smaller value indicates higher prediction accuracy. After training and testing, the prediction effect and prediction error of i_{ref} are shown in Fig. 16. The root mean square error of the prediction is 0.11342.

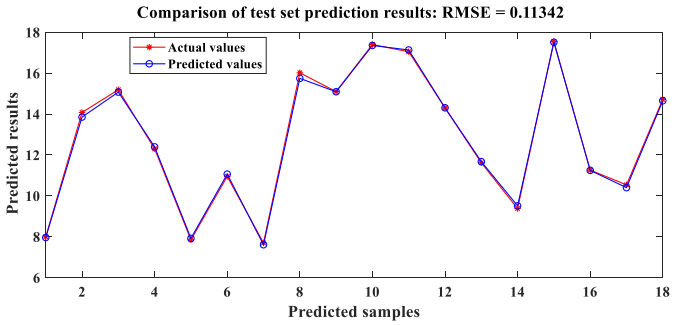

FIGURE 16. Curve chart of i_{ref} prediction effect.

4. SIMULATION ANALYSIS

To verify the current-torque synergy DITC proposed in Section 3, a simulation model of 6/20 PMa-SRM is built in Matlab/Simulink, and comparative tests are conducted on the traditional DITC and current-torque synergy DITC, and the prototype parameters are shown in Table 1.

TABLE 1. Motor parameters.

Parameter	Value	Parameter	Value
Number of stator poles	6	Number of stator poles	6
Number of rotor poles	20	Number of rotor poles	6
Winding turns	55	Winding turns	3
Shaft length (mm)	100	Shaft length (mm)	540
Rotor outer diameter (mm)	172	Rotor outer diameter (mm)	30
Stator outer diameter (mm)	142	Stator outer diameter (mm)	0
Air gap length (mm)	0.6	Air gap length (mm)	8
Rotor pole width (mm)	6	Rotor pole width (mm)	3

In order to better compare the effects of the traditional DITC and the current-torque synergy DITC in suppressing torque ripple, the torque ripple coefficient K_r is defined as follows:

$$K_r = \frac{T_{\max} - T_{\min}}{T_{av}} \times 100\% \tag{7}$$

In the formula, $T_{\max}$, $T_{\min}$, and T_{av} represent the maximum torque, minimum torque, and average torque output by the system when it is stable, respectively.

Compared with the traditional DITC, the current-torque synergy control DITC is more capable of reducing the current peak and suppressing the torque pulsation. As shown in Fig. 17, for a given speed of 300 r/min and a load torque of 2 N-m, the current-torque co-control DITC reduces the peak current from 8.7 A to 8.0 A and the torque pulsation from 24% to 19%.

When the speed is increased to 500 r/min and the load torque increased to 5 N·m, the simulated waveforms under the two control strategies are shown in Fig. 18. It can be seen from the figure that the current peak of the traditional DITC is 14.9 A; the output torque ranges from 4.85 to 6.10 N·m; the torque ripple is approximately 1.25 N·m; and the torque ripple coefficient is 25%. In contrast, the current peak of the current-torque synergy DITC is 12.6 A; the output torque ranges from 4.90 to 5.25 N·m; the torque ripple is approximately 0.35 N·m; and the torque ripple coefficient is 7%.

In traditional DITC, the exciting phase current rises too rapidly in the commutation region, causing electromagnetic torque to surge and exceed the demagnetizing phase torque reduction, leading to excessive ripple. By contrast, the current-torque synergy DITC controls exciting phase current in Commutation Zone I and keeps the demagnetizing phase in the "−1" state as much as possible in Zone II to prolong demagnetization time, resulting in smoother three-phase synthesized torque output and smaller ripple.

When the speed is increased to 1000 r/min and the load torque increased to 8 N-m, as can be observed from Fig. 19,

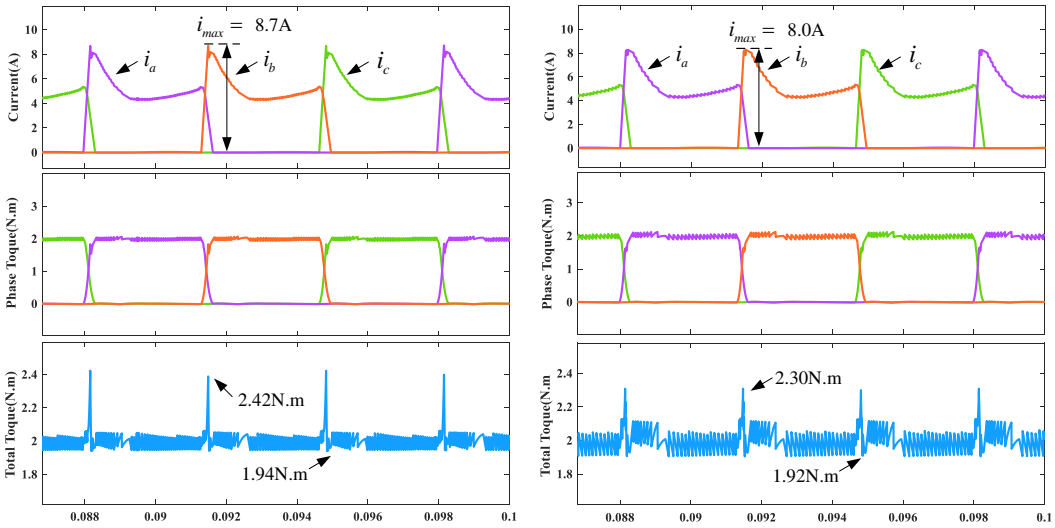

FIGURE 17. Current and torque waveforms of traditional DITC and current-torque synergy DITC (300 r/min, 2 N·m).

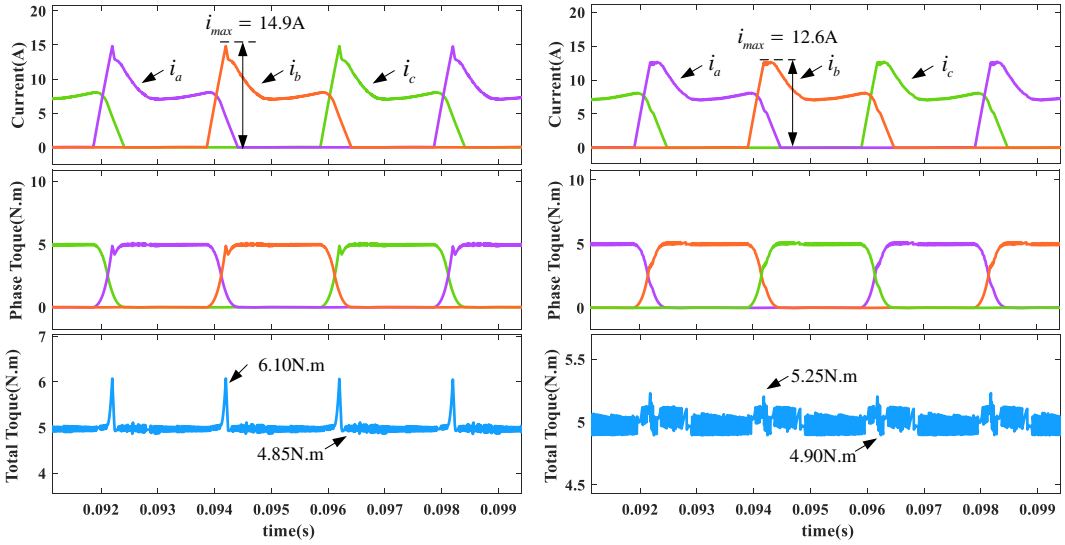

FIGURE 18. Current and torque waveforms of traditional DITC and current-torque synergy DITC (500 r/min, 5 N·m).

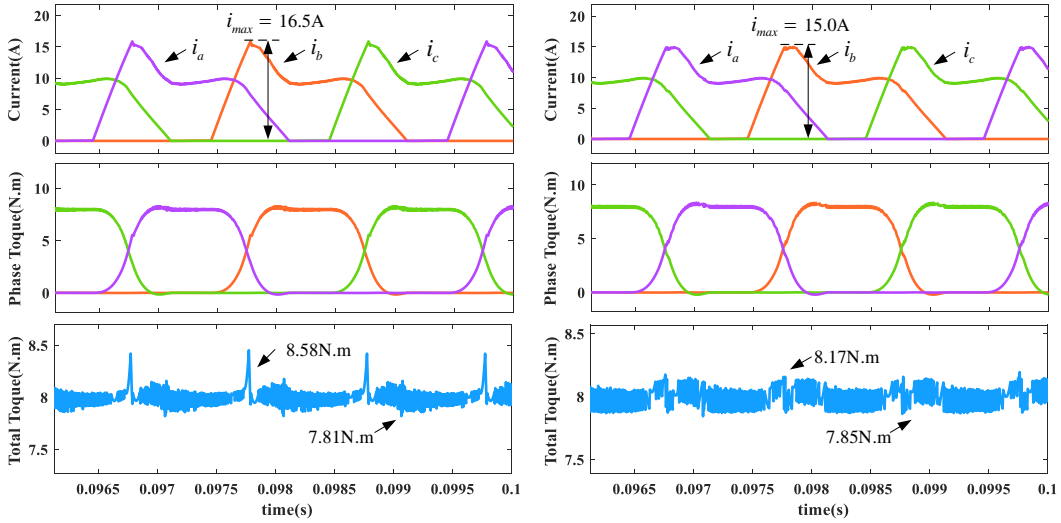

FIGURE 19. Current and torque waveforms of traditional DITC and current-torque synergy DITC (1000 r/min, 8 N·m).

the current peak of the traditional DITC is 16.5 A, with the output torque ranging from 7.81 to 8.58 N·m. The torque ripple is approximately 0.77 N·m, and the torque ripple coefficient is 9.63%. In contrast, the current peak of the current-torque synergy DITC is 15.5 A; the output torque spans from 7.85 to 8.17 N·m; the torque ripple is 0.32 N·m; and the torque ripple coefficient is 4%.

Traditional DITC uses only torque error hysteresis for the exciting phase, lacking current control and causing instant torque surges at inductance breakpoints, leading to sharp ripples. The current-torque synergy DITC applies current chopping to exciting phases with weak torque but fast current rise in early commutation, and torque hysteresis control to demagnetizing phases with strong torque output. This reduces current peaks and avoids large torque fluctuations during commutation. The simulation results under different speeds and loads are shown in Table 2 and Table 3.

TABLE 2. Traditional DITC operation at different speeds and loads.

Speed (r/min)	Load (N·m)	I_{max} (A)	K_r(%)
300	2	8.7A	24%
300	5	15.5A	20%
300	8	18.5A	16%
500	2	8.1A	22%
500	5	14.9A	25%
500	8	17A	17.5%
1000	2	7.8A	20%
1000	5	14A	12%
1000	8	16.5A	9.65%

TABLE 3. Current-torque synergy DITC operation at different speeds and loads.

Speed (r/min)	Load (N·m)	I_{max} (A)	K_r (%)
300	2	8.0A	19%
300	5	12.8A	12%
300	8	16.2A	7%
500	2	7.6A	16%
500	5	12.6A	7%
500	8	15.5A	3.75%
1000	2	7.4A	14%
1000	5	12.2A	5%
1000	8	15A	4%

5. EXPERIMENTAL VALIDATION

To further verify the feasibility of the current-torque DITC method, an experimental platform with a 6/20 PMa-SRM motor speed control system as the core was built as shown in Fig. 20. The experimental platform consists of a mechanical part and an electrical part, where the mechanical part is composed of a PMa-SRM prototype, a coupling, a torque sensor, and a magnetic powder brake, and the electrical part is composed of a DSP TMS320F28335, a three-phase asymmetric power converter, a 15-bit absolute position encoder, and a current clamp. Real-time torque and speed are transmitted to the host computer via the torque sensor.

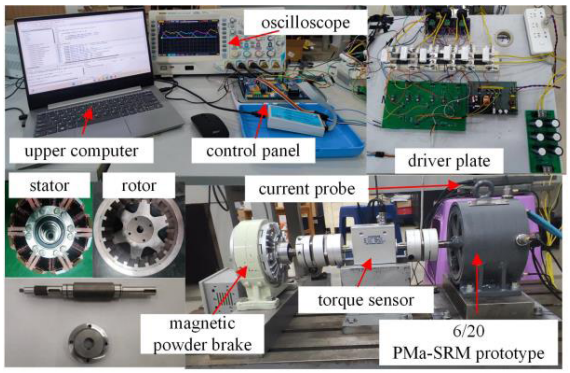

FIGURE 20. Control system experiment platform.

In order to verify the effectiveness of the current-torque synergistic DITC, it is tested under the operating conditions with a given speed of 300 r/min and a load torque of 2 N·m, as shown in Fig. 21 and Fig. 22. From the figures, it can be seen that the peak current of the conventional DITC is 10.0 A, and the torque ripple is 37%. In the case of current-torque synergistic DITC, the peak current is 9.0 A, and the torque ripple is 21%.

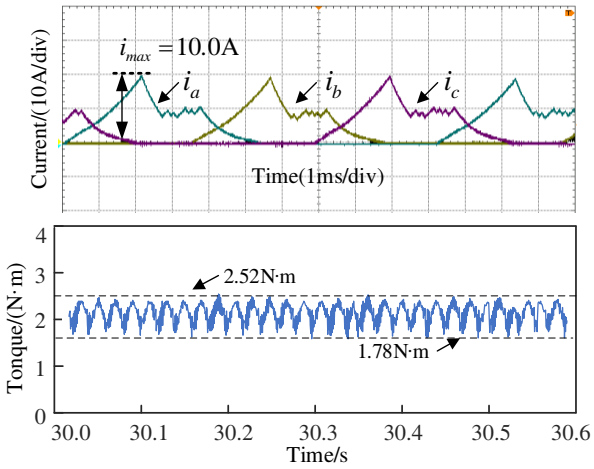

FIGURE 21. Current and torque waveform diagrams of traditional DITC (300 r/min, 2 N·m).

When the rotational speed is 500 r/min, and the load is 5 N·m, the comparative experimental diagrams of the prototype under traditional DITC and current-torque synergy DITC are shown in Fig. 23 and Fig. 24. It can be seen from the figures that traditional DITC only relies on torque error as the switching criterion for the exciting phase and cannot control the rapid rise of current. Meanwhile, excessive current generates larger instantaneous torque at the inductance breakpoints, further increasing torque ripple. In contrast, the dual-vector DITC subdivides the TpE region into TpE Zone I and TpE Zone II according to inductance characteristics, and controls the exciting current in TpE Zone I, reducing the current peak from 14.0 A to 11.8 A and the torque ripple from 31.8% to 16%.

When the rotational speed increases to 1000 r/min, and the load rises to 8 N·m, prototype experiments comparing tradi-

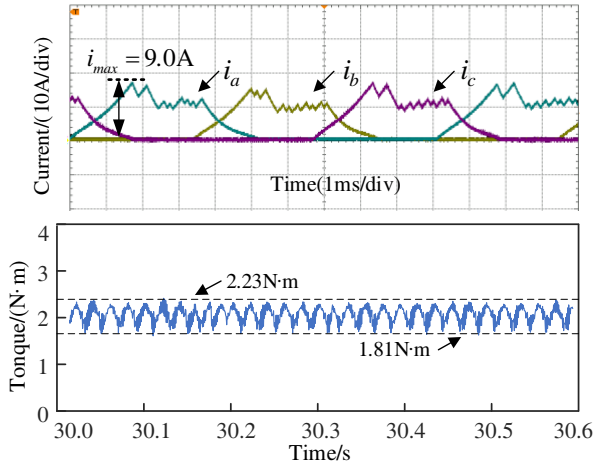

FIGURE 22. Current and torque waveform diagrams of current-torque synergy DITC (300 r/min, 2 N·m).

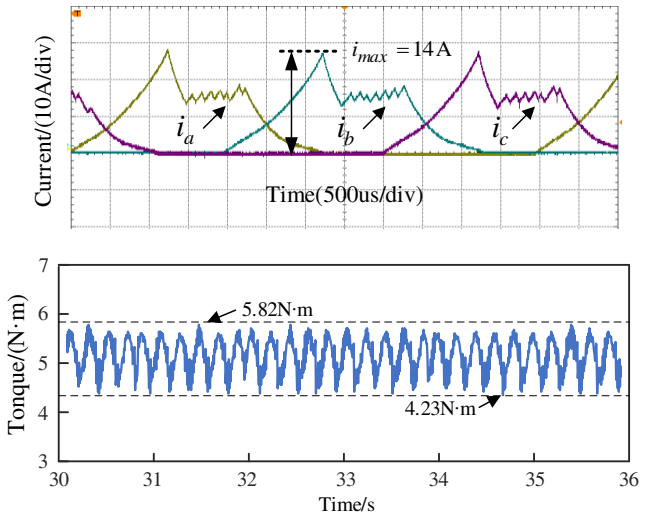

FIGURE 23. Current and torque waveform diagrams of traditional DITC (500 r/min, 5 N·m).

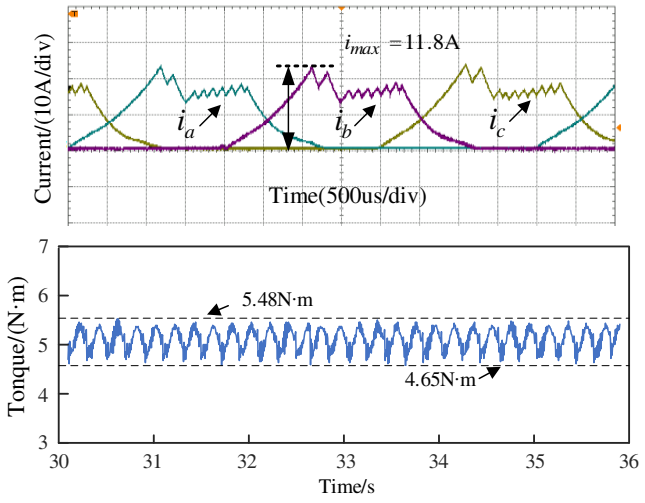

FIGURE 24. Current and torque waveform diagrams of current-torque synergy DITC (500 r/min, 5 N·m).

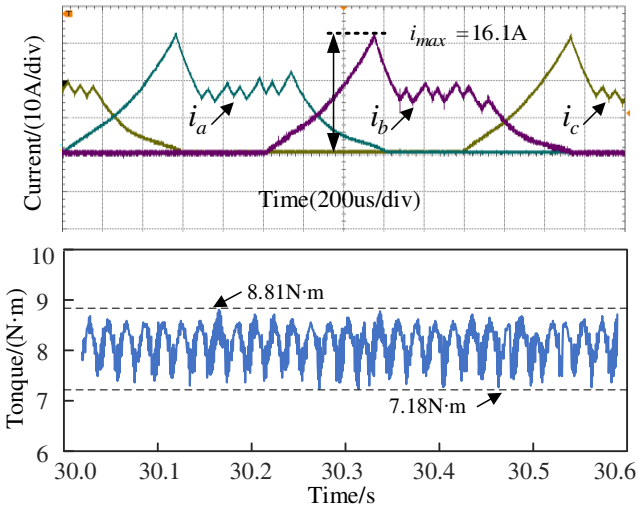

FIGURE 25. Current and torque waveform diagrams of traditional DITC (1000 r/min, 8 N·m).

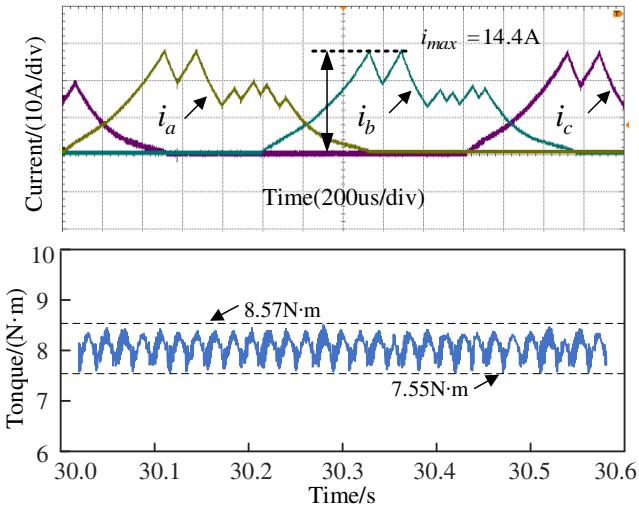

FIGURE 26. Current and torque waveform diagrams of current-torque synergy DITC (1000 r/min, 8 N·m).

tional DITC and current-torque synergy DITC are shown in Figs. 25 and 26. Compared with traditional DITC, the current-torque synergy DITC reduces the current peak from 16.1 A to 14.4 A and the torque ripple from 20.3% to 12.7%. Results show that the proposed strategy effectively suppresses current pulses and reduces torque ripple.

6. CONCLUSION

To address the issues of high current pulses and large torque ripple in traditional DITC, this paper proposes a current-torque synergy DITC control strategy. Based on inductance characteristics, the strategy subdivides the TpE region of traditional DITC into TpEI and TpEII zones. It uses two vectors of current error and torque deviation as new switching criteria and optimizes the control strategy within each zone to reduce both torque ripple and current peaks. Simulated and experimental results verify the effectiveness and correctness of the proposed method.

ACKNOWLEDGEMENT

This work was supported by the National Natural Science Foundation of China Grant No. 52167005, in part by the Jiangxi Provincial Key Laboratory of Maglev Rail Transit Equipment under No. 2020SSY050, and in part by the Jiangxi Natural Science Foundation Project under 20232BAB204063.

REFERENCES

[1] Kusumi, T., K. Kobayashi, K. Umetani, and E. Hiraki, "Analytical derivation of phase-current waveform for elimination of torque and input-current ripples of switched reluctance motor operating under magnetic saturation," *IEEE Transactions on Industry Applications*, Vol. 58, No. 4, 5248–5261, 2022.

[2] Ding, W., J. Li, and J. Yuan, "An improved model predictive torque control for switched reluctance motors with candidate voltage vectors optimization," *IEEE Transactions on Industrial Electronics*, Vol. 70, No. 5, 4595–4607, 2023.

[3] Yu, Z., C. Gan, K. Ni, Y. Chen, and R. Qu, "A simplified PWM strategy for open-winding flux modulated doubly-salient reluctance motor drives with switching action minimization," *IEEE Transactions on Industrial Electronics*, Vol. 70, No. 3, 2241–2253, 2023.

[4] Jing, B., X. Dang, Z. Liu, and S. Long, "Torque ripple suppression of switched reluctance motor based on fuzzy indirect instant torque control," *IEEE Access*, Vol. 10, 75 472–75 481, 2022.

[5] Rana, A. K. and A. V. R. Teja, "A mathematical torque ripple minimization technique based on a nonlinear modulating factor for switched reluctance motor drives," *IEEE Transactions on Industrial Electronics*, Vol. 69, No. 2, 1356–1366, 2022.

[6] Röth, C., F. Milde, D. Trebbels, J. Schmidt, and M. Doppelbauer, "A stator with offset segments and a double stator design for the reduction of torque ripple of a switched reluctance motor," *IEEE Transactions on Energy Conversion*, Vol. 37, No. 2, 1233–1240, 2022.

[7] Davarpanah, G. and J. Faiz, "A novel structure of switched reluctance machine with higher mean torque and lower torque ripple," *IEEE Transactions on Energy Conversion*, Vol. 35, No. 4, 1859–1867, 2020.

[8] Choi, Y. K., H. S. Yoon, and C. S. Koh, "Pole-shape optimization of a switched-reluctance motor for torque ripple reduction," *IEEE Transactions on Magnetics*, Vol. 43, No. 4, 1797–1800, 2007.

[9] Sohrabzadeh, A., H. Torkaman, and A. Y. Javid, "Improvement undesirable characteristics of the switched reluctance motor with triangular rotor structure," *IEEE Transactions on Energy Conversion*, Vol. 38, No. 3, 2118–2125, 2023.

[10] Yasa, Y., Y. Sozer, and M. Garip, "Acoustic noise mitigation of switched reluctance machines with leaf springs," *IEEE Transactions on Industrial Electronics*, Vol. 70, No. 2, 1250–1260, 2023.

[11] Chen, Y., Q. Jiang, J. Wang, and W. Yao, "Current chopping control strategy of switched reluctance motor based on inductance characteristics," *Journal of Beijing University of Aeronautics and Astronautics*, Vol. 49, No. 3, 647–656, 2023.

[12] Meng, F. G., W. P. Zhang, A. M. Liu, *et al.*, "Current control method to suppress SRM torque ripple," *Electric Machines and Control*, Vol. 26, No. 9, 49–56, 2023.

[13] Ren, H., C. Gan, R. Qu, S. Wang, and J. Sun, "Current-torque coordinated control based direct instantaneous torque control strategy for switched reluctance motor," *Proceedings of the CSEE*, Vol. 44, No. 19, 7794–7805, 2023.

[14] Huang, C. Z., J. X. Xu, X. P. Liu, *et al.*, "A four region DITC method for permanent magnet assisted switched reluctance motor," *Proceedings of the Chinese Society for Electrical Engineering*, Vol. 43, No. 06, 2438–2450, 2023.

[15] Cai, Y., C. Ju, H. Wang, *et al.*, "A new direct instantaneous torque control method of switched reluctance motor and its high efficiency operation," *Transactions of China Electrotechnical Society*, Vol. 37, No. 18, 4625–4637, 2022.

[16] Sun, Q., J. Wu, and C. Gan, "Optimized direct instantaneous torque control for SRMs with efficiency improvement," *IEEE Transactions on Industrial Electronics*, Vol. 68, No. 3, 2072–2082, 2021.

[17] Cai, H., H. Wang, M. Q. Li, and M. Li, "Predictive current control of switched reluctance motor for torque ripples minimization," *Proceedings of the CSEE*, Vol. 39, No. 16, 4899, 2019.

[18] Huang, C., Y. Sun, J. Xu, and H. Li, "A novel direct instantaneous torque control strategy in permanent magnet-assisted switched reluctance motor based on optimization of conduction angle," *Alexandria Engineering Journal*, Vol. 105, 120–129, 2024.